Energy Storage Materials 41 (2021) 546–553

Contents lists available at ScienceDirect

Energy Storage Materials

journal homepage: www.elsevier.com/locate/ensm

Lithium distribution and transfer in high-power 18650-type Li-ion cells at multiple length scales

Dominik Petz[a,b], Martin J. Mühlbauer[b,c], Volodymyr Baran[b,d], Alexander Schökel[b,c,d], Vladislav Kochetov[a,e], Michael Hofmann[b], Vadim Dyadkin[f,g], Peter Staron[h], Gavin Vaughan[g], Ulrich Lienert[d], Peter Müller-Buschbaum[a,b], Anatoliy Senyshyn[b,*]

[a] Lehrstuhl für Funktionelle Materialien, Physik-Department, Technische Universität München, James-Franck-Str. 1, 85748 Garching, Germany
[b] Heinz Maier-Leibnitz Zentrum (MLZ), Technische Universität München, Lichtenbergstrasse 1, 85748 Garching, Germany
[c] Institute for Applied Materials (IAM), Karlsruhe Institute of Technology (KIT), Hermann-von-Helmholtz-Platz 1, 76344 Eggenstein-Leopoldshafen, Germany
[d] Deutsches Elektronen Synchrotron (DESY), Notkestr. 85, 22607 Hamburg, Germany
[e] Institut für Physik, Universität Rostock, A.-Einstein-Str. 23-24, 18059 Rostock, Germany
[f] Swiss-Norwegian Beam Lines, ESRF-The European Synchrotron, 71, Avenue des Martyrs, 38042 Grenoble Cedex 9, France
[g] ESRF-The European Synchrotron, 71, Avenue des Martyrs, 38042 Grenoble Cedex 9, France
[h] Helmholtz-Zentrum Hereon, Max-Planck-Str. 1, 21502 Geesthacht, Germany

ARTICLE INFO

Keywords:
In operando neutron diffraction
Graphite anode
Lithium homogeneity
Spatially-resolved diffraction
X-ray diffraction tomography
Depth lithium profile

ABSTRACT

The distribution of lithium inside electrodes of a commercial Li-ion battery of 18650-type with $LiFePO_4$ cathode and graphite anode is investigated on different length scales using neutron diffraction, X-ray (synchrotron-based) diffraction and X-ray computed tomography. Evolution of 2D (in-plane) lithium distribution in lithiated graphite is monitored during charge/discharge using millimeter-sized spatial resolution. Micrometer-sized details of cell organization and lithiation of both the positive and negative electrodes are obtained from diffraction-based tomography applying synchrotron radiation. In-situ lithiation of the cathode over its thickness and development of the lithium concentration front during cell charge/discharge is traced by diffraction-based profiling with a micrometer-sized synchrotron beam in a single-layer electrochemical cell.

1. Introduction

Lithium-ion batteries enter our daily life more and more since their commercialization in 1991. Their outstanding energy/power density compared to other electrochemical energy storage systems available on the market [1] makes Li-ion batteries dominant in the segment of energy storage for portable electronics and electric drivetrains. Despite its overall popularity the Li-ion technology still raises certain concerns, e.g. in terms of safety [2] and performance fading [3].

The safety of Li-ion cells depends on a variety of microscopic factors maintaining the integrity of the cell. Chemical, mechanical and morphological uniformity of the cell components is crucial for optimization, estimation and prediction of cell parameters and cell behavior during standard operation and misuse. “Real-life” cells are complex, closed systems exhibiting non-uniform distributions of lithium, electrolyte, salt or other components that highly depend on the state-of-charge (SOC) of the cells and properties like capacity, current, temperature, pressure, etc. Cell aging leads to the development of a heterogeneous distribution of battery parameters, which are often hard to predict by modeling and require experimental input based on complex characterizations.

Selected methodologies for probing the uniformity of cell components are briefly reviewed in Ref. [4]. A number of microscopy [5], spectroscopy [6] or scattering-based [7,8] techniques can be applied for *ex-situ* analysis of cell components, mainly active electrode materials. If non-destructive methods have to be applied (due to closed system features), imaging [9,10] and diffraction experiments [11] using either neutrons or synchrotron radiation are the optimal choice to examine instrument-adopted test cells [12] or commercially available large format Li-batteries [13,14]. In recent years a number of methods to combine imaging and diffraction have been developed, either in the form of Bragg-imaging [15], spatially-resolved diffraction [16] or computed tomography using an X-ray diffraction signal (XRD-CT) instead of attenuation (X-ray CT) [17]. The XRD-CT method has created a kind of new non-destructive insight with unprecedented sensitivity and contrast [18-20] and is currently under active development.

When classifying Li-ion cells according to lithium uniformity, it was shown [21,22] that cells optimized for high-power applications display

* Corresponding author.
E-mail address: anatoliy.senyshyn@gmail.com (A. Senyshyn).

https://doi.org/10.1016/j.ensm.2021.06.028
Received 14 May 2021; Received in revised form 14 June 2021; Accepted 20 June 2021
Available online 23 June 2021

a systematically higher lithium heterogeneity level compared to high energy cells. Among them, the ANR18650-M1A cell, which adopts $LiFePO_4$ (LFP) as cathode and graphite (C) as anode, is quite remarkable: It exhibits an unusual configuration of current lids optimized for low internal resistance and high-power output resulting in a non-uniform current density profile along the electrode stripe; it displays a very narrow range of constant lithium concentration (plateau) in the fully charged state and also a cell height dependent lithiation profile. In such cells, the heterogeneous lithium distribution is a direct consequence of the cell layout optimized for remarkably high charge/discharge rates (normal/fast charging 1.5C/4.5C; normal/peak discharging 27C/55C).

Cells of similar type have already been investigated in various studies using electrochemical characterization and impedance spectroscopy [23], theoretical simulations [24] and thermophysical characterization [25]. Details of lithium intercalation in $LiFePO_4$ [26,27] and aging behavior have been investigated using synchrotron radiation (either in monochromatic [28] or energy-dispersive [29] mode) and neutron diffraction [30], where a high cycling stability at high charging rates was observed in LFP|C cells. Recently, a capacity recovery effect of up to 10% after continuous shallow cycling reported for APR18650-M1A cells [31] has been attributed to more heterogeneous lithium distributions in the electrodes during fast cycling.

Therefore, a detailed study of the lithium distribution in high-power Li-ion batteries based on a LFP|C cell chemistry will contribute to the improved understanding of the important type of lithium-ion batteries. In the present work we focus on monitoring the uniformity of the graphite lithiation in a high-power LFP|C cylinder-type cell during cell charge/discharge as well as probing the lithium distribution in a LFP|C cylinder-type cell non-destructively on μm scale in the fully charged state. The work is based on our systematic studies of lithium uniformity in "real-life" Li-ion batteries using a combination of diffraction and imaging methods along with electrochemical characterization.

2. Experimental methods

2.1. Spatially resolved neutron powder diffraction

A fresh lithium-ion battery (18650-type cylinder, ANR18650-M1A[1], A123 systems) with LFP|C chemistry was electrochemically charged/discharged, while diffraction data were collected non-destructively by spatially-resolved neutron powder diffraction.

Cell charging/discharging was carried out using a SP-240 potentiostat from BioLogic applying a CCCV-charge/discharge protocol. The constant current was set to 2 A (approx. 2C) for both charging and discharging between the lower voltage limit of 2.0 V and the upper limit of 3.6 V, covering the full voltage range of the battery. The cut-off current for the CV phase was set to 55 mA (~C/20) as a good compromise between cycling time, neutron exposure and cell relaxation. The measurements started in the fully discharged state.

The spatially-resolved neutron powder diffraction experiments were carried out at the materials science diffractometer STRESS-SPEC [32] (FRM II, Garching b. München, Germany). The incoming neutron beam with a wavelength of λ=1.615 Å obtained from a 311 Ge monochromator was formed to 2 mm width and 17 mm height by a slit system in front of the sample. A 2D-detector (^{3}He position sensitive, 250×250 mm^2, 256×256 pixels) was placed at a distance of 1056 mm from the sample position and a central angle of ≈27° in 2θ. A radial oscillating collimator with a fixed field of view of 2 mm was placed in front of the detector. In combination with the incoming beam, a gauge volume with a rhomb-like planar cross-section is formed (Fig. S1 a, b). Combined sample rotation and translation allowed for a relative movement of the gauge volume throughout the whole cell volume, scanning a horizontal plane enabling a 2D reconstruction of the lithium distribution.

The exposure time per pattern was 300 s, while the diffraction data was acquired continuously during a full cell charge/discharge cycle per gauge volume. The start and stop points of the data collection per single gauge volume were externally triggered by the potentiostat. Altogether, diffraction data were collected for 32 gauge volumes covering half of the cell (Fig. S1c). Taking into account a rotational symmetry for this type of 18650-type cell (see cell #34 in [33]), these data are sufficient for the reconstruction of the phase composition of the lithiated graphite anode and, correspondingly, the lithium concentration x in Li_xC_6. The evolution of diffraction patterns for selected gauge volumes is plotted in Figs. S2.

2.2. High-resolution neutron powder diffraction

Structural characterization of the entire cell was performed using the high-resolution neutron powder diffractometer SPODI (FRM II, Garching b. München, Germany) [34,35] and monochromatic neutrons with a wavelength of 1.5482 Å (551 Ge monochromator, vertically focusing, 155 deg. take-off angle). The 18650-type cell was mounted on the sample table of the diffractometer and the data collection was performed at SOC = 0 % and 100 % (see Figs. S3). With a sample slit opening of 40×20 mm (v x h) in front of the sample, the irradiated cell volume corresponds to ca. 85% of the whole electrode material, where the diffraction data reflects an average over the irradiated volume. Due to the different scattering power of the cell components, the contribution from the LFP cathode to the neutron powder diffraction pattern is rather small and the majority of the signal is due to graphite, cell housing and current collectors (Fig. S4).

2.3. X-Ray computed tomography (X-ray CT): attenuation based

The internal cell layout of the studied cell was examined by X-ray CT using a v|tome|x s 240 tomography scanner (General Electric). The direct tube was used at a voltage of 130 kV and a current of 100 μA. Data collection was carried out in cone beam geometry with a high-resolution amorphous silicon 2D detector (200×200 mm^2, 1000×1000 pixels). The magnification was adjusted to get an effective pixel size of 40 μm. For every sample two data sets of 1001 projections each were collected, where each projection corresponds to an average of 3 single exposures of 1000 ms. The reconstruction was performed with the phoenix datos|x software. Two 3D datasets (top and bottom part) were merged for every cell using the software ImageJ [36]. The final visualization of the data, including the separation/segregation and color coding of the different parts, was carried out in VGStudio MAX from VolumeGraphics.

2.4. X-Ray diffraction radiography (XRDR)

The X-ray diffraction radiography studies were carried out using synchrotron radiation at the id11 beamline (ESRF, Grenoble, France) [37] and the P02.1 beamline (PETRA III at DESY, Hamburg, Germany) [38]. At id11, the experiment was using a photon beam with a wavelength of $\lambda \approx 0.18$ Å and a diameter of ca. 10 μm. The data collection geometry was similar to the reported one in Ref. [4]. The scan was performed over the whole cell height with 0.25 mm steps. The 2D diffraction data were collected using a Frelon position-sensitive detector and integrated using Bubble package [39]. A typical diffraction pattern is presented in Fig. S5. Broad reflections with double peak features were attributed to the pronounced self-collimation effect caused by large sample/cell diameter. At P02.1 the experiment was carried out using a photon energy of 60 keV, beam size of ca. 1×1 mm^2 and sample-to-detector distance of ca. 2.4 m. 2D diffraction data were collected using a 16-inch (~409.6 mm) 2D flat panel detector of the XRD 1621N ES Series (PerkinElmer) with 2048×2048 pixels and a pixel size of 200×200 μm^2. Masking and radial detector integration was carried out using Dioptas

[1] Nominal capacity 1100 mAh (observed: 995-1005 mAh); voltage window 2.0-3.6 V; nominal charge/discharge range (CC) 4/30 A

[40]. An exemplary diffraction pattern is presented in Fig. S5. Besides this, the evolution of the diffraction signal vs. electrochemical state of the cell was measured along center lines of the cell in vertical and horizontal direction. A stack of diffraction data with color-coded intensity is shown in Fig. S6.

2.5. X-Ray diffraction computed tomography (XRD-CT)

The X-ray diffraction computed tomography experiment was carried out at id15A beamline (ESRF, Grenoble, France) [41]. The photon beam was focused and shaped down to a beam dimension of 30×30 μm^2. A wavelength of $\lambda \approx 0.18$ Å was used as a compromise between the absorption of the sample and the resolution of the diffraction data. 2D data were collected using a flat PerkinElmer 2D detector with 2048×2048 pixels and a pixel size of 200×200 μm^2. The XRD-CT data collection was performed using a standard "scanning" approach (continuous traverse scan and stepped angular scan according to [42]) comprised of 660 translations over the range of [-9.9 : 9.9] mm and 420 rotation steps covering [-94.5:94.5] deg. A diffraction pattern, obtained by averaging over 660×420 = 277200 collected patterns, is plotted in Fig. S7d. Radial integration of the dataset was carried out using Bubble software [39]. The reconstruction of the integrated diffraction intensities was performed in Matlab using the embedded inverse Radon transform algorithm.

2.6. Spatially-resolved X-ray diffraction using conical slits

Spatially-resolved diffraction experiment with conical-slits was performed at the HEMS (P07) beamline (PETRA III at DESY, Hamburg, Germany) [43]. The sample was mounted on a sample goniometer enabling translation and rotation. A PerkinElmer XRD 1621 fast area detector with 2048×2048 pixels of 200×200 μm^2 size at a sample distance of 2.403 m was used for data collection. In front of the sample, a slit system [44] was used to shape the incoming photon beam to a size of 100×100 μm^2. An optimal wavelength of λ=0.20838 Å matching the 001 reflection from LiC_6 and the 002 reflection from LiC_{12} with the first opening of the conical slits (see Fig. S8a) was chosen. With such configuration, a needle-like gauge volume of ca. 0.1×0.1×1.03 mm^3 was selected and data were collected on the predefined mesh (Fig. S8b).

2.7. Depth-resolved XRD scans using μm-sized beam

A piece of the double-coated LFP cathode was extracted from the 18650-type cell and cleaned on one side to obtain a single-coated layer, which was punched to a circular shape with 2 mm in diameter and mounted in a compact *in-situ* cell designed for high-energy X-ray diffraction. A sketch of the cell in the form of an exploded view is shown in Fig. S9. The cell was mounted at the sample table of the P21.2 beamline (PETRA III (DESY), Hamburg, Germany) [45] and aligned using a silicon diode in the primary beam. The monochromatic high-energy photon beam with a wavelength of $\lambda \approx 0.23$ Å was focused to 3×6 μm^2 (v x h). The scan was performed in vertical direction (in accordance with the scheme shown in Fig. S9) using 2 μm steps. 2D diffraction data was collected at each step using a PILATUS 2M detector in continuous mode with 0.3 s per exposure. Masking and radial detector integration was carried out using Dioptas [40]. The cell was galvanostatically cycled with a VMP3 potentiostat from BioLogic in the voltage range of 2.5 - 3.6 V using a current of ±10.8 μA corresponding to a C-rate of 1C.

3. Data analysis

3.1. Neutron diffraction

The collected 2D diffraction patterns were corrected with respect to detector nonlinearities, geometrical aberrations and curvature of the Debye-Scherrer rings. The corrected 2D diffraction data were integrated to get 1D diffraction patterns (intensity vs. scattering angle), whose angular 2θ coverage depended on the type of the diffraction experiment. Rietveld refinement was applied for the high-resolution data sets (Fig. S3), whereas the limited 2θ range in the spatially-resolved neutron powder diffraction experiment (described in Section 2.1) did not enable the use of Rietveld refinement for the analysis. This method was also not accessible in the XRDR (Section 2.4) and XRD-CT (Section 2.5) experiments due to the complex peak shape caused by beam self-collimation on a sample. This limited the analysis procedure to the consideration of integral intensities, which, if properly analyzed, can be used as sensitive and non-destructive indicators for lithiation of electrode materials [4]. The diffraction data obtained by neutron scattering is dominated by the signal from the negative electrode (graphite), whereas the Bragg peaks characteristic to the cathode are usually stronger in X-ray and synchrotron diffraction data (Fig. S4).

In the charged state, the x in Li_xC_6 can be calculated directly from the diffraction data using integral intensities of the 001 and 002 reflections for lithiated graphites in stage I (LiC_6) and stage II (LiC_{12}) [33], respectively. For the sake of simplicity, the obtained mean lithium concentration x in Li_xC_6 can be transferred into the degree of lithiation (DoL). At 0.5<DoL<1.0 the lithiation of the graphite exhibits a biphasic behavior formed by stage I and stage II [46,47]. At DoL<0.5 the biphasic mode switches to a *quasi*-solid solution behavior, which is supplemented by the decomposition of stage I [46,47]. Further delithiation results in the formation of phases $Li_{x<0.5}C_6$ in different mixtures until the lithium-free graphite (C_6 = 6C) phase is reached. These changes in DoL are directly reflected in the diffraction patterns (Fig. S2) in the form of a modulation of the diffraction intensity and a shift of the Bragg reflection towards higher scattering angles corresponding to a quasi-continuous transformation from LiC_{12} to C_6 [46,47]. Since the mixture of the phases $Li_{x<0.5}C_6$ cannot be resolved in detail from the medium – resolution diffraction patterns, a simplified and more general approach needs to be implemented.

Every diffraction pattern obtained in the spatially-resolved neutron diffraction experiment (Fig. S2) can be unambiguously correlated to the electrochemical data, e.g. established cell capacity. The relative cell capacity (represented in SOC by %) in turn is correlated to the DoL of graphite, where at SOC = 0 % one expects DoL = 0 (pure graphite phase) and at SOC = 100 % the DoL = 0.838 (maximal value for the stage I and stage II mixture in the reference data) is obtained using the method described in Ref. [33]. Assuming the amount of intercalated lithium to be proportional to the cell capacity, one can create a lookup table connecting the "mean" diffraction behavior with the DoL, from which the DoL can also be obtained for mixed phases with $Li_{x<0.5}C_6$ in the solid-solution range. In the latter case the DoL is also reflected in the scattering angle of the corresponding $Li_{x<0.5}C_6$, phase ranging between 002 of LiC_{12} and 002 of pure graphite. The maximum value for the DoL in the solid-solution range is 0.5 corresponding to the LiC_{12} phase, in which every second (50%) layer of lithium between the graphite sheets is occupied.

Both the DoL and the diffraction data (in the form of integrated peak intensities for a series of phases) can be related by a simple relationship

$$n_i = w_i I_i \tag{1}$$

$$\mathrm{DoL} = \frac{n_{LiC_6}}{n_{LiC_6} + n_{Li_{x\leq 0.5}C_6} + n_{C_6}} + \frac{n_{Li_{x\leq 0.5}C_6}}{n_{LiC_6} + n_{Li_{x\leq 0.5}C_6} + n_{C_6}} L(2\theta) \tag{2}$$

where the first and second terms in (2) illustrate the biphasic and solid-solution regimes, I is the integrated intensity of the corresponding phase (either LiC_6, $Li_{x<0.5}C_6$, or non-lithiated carbon C_6). The L is obtained from the lookup table and it is a coefficient relating to the DoL and the scattering angle of the corresponding reflection for the $Li_{x<0.5}C_6$ phase, with a maximal value of 0.5 corresponding to pure LiC_{12}. The diffraction intensities I have to be weighted by a factor of $w_i = [V_i/F_{hkl}]^2[\rho_i/M_i]$, where V_i is the unit cell volume, F_{hkl} the structure factor, ρ_i the density and M_i the molar mass of the corresponding phase i and Miller-

Table 1
Selected parameters of $FePO_4$ and $LiFePO_4$ used in the quantitative phase analysis of X-ray data

	$FePO_4$	$LiFePO_4$	LiC_6	LiC_{12}
Cell volume V, Å^3	271.924	287.231	59.676	112.284
Molar mass M, g/mole	150.8164	157.7574	79.007	151.073
Crystallographic density ρ, g/cm^3	3.056	3.470	2.2	2.23
Structure factor F^2				
200 reflection	5682	5382		
301 reflection	2553	2777		
001 reflection			642.3	
002 reflection				2571.9

indices *hkl*, which results from an approximation of diffraction intensity of neighbouring diffraction peaks [48]. Taking into account a series of Li_xC_6 phases occurring during the graphite lithiation [47] an approximation of weighting factors was applied (Fig. S10).

The introduction of the DoL has a series of advantages for combining the biphasic and solid-solution like behavior regimes of the lithium intercalation.

3.2. X-Ray diffraction tomography

In the XRD-CT experiment (Section 2.5), the final diffraction patterns were obtained in an angular range of 0.5-10.0 deg. Because of strong self-collimation caused by the cell dimension in the beam direction, the integral peak intensities were reconstructed instead of diffraction intensities vs. 2θ as proposed in Refs. [42,49]. Several characteristic reflections describing separator (d=8.52 Å), cathode (200 $LiFePO_4$, 200 $FePO_4$), anode (001 LiC_6, 002 LiC_{12}), current collectors (111 Cu, 111 Al) and cell housing (110 Fe) were chosen and their integral intensities were calculated from the background-subtracted experimental diffraction patterns. The anode signal was composed of reflections from LiC_6 and LiC_{12}, whereas the cathode signal corresponds to $FePO_4$ with minor traces of $LiFePO_4$, which is in line with the fully charged state of a LFP|C chemistry subjected to XRD-CT [28].

The reconstructed intensities of the characteristic reflections unambiguously enabled the localization of cell housing, center pin, current collectors, electrode stripes and separator (Fig. S11). The biphasic character (Fig. S6) of the intercalation mechanism in the LFP cathode and the graphite anode (when lithiated above 50% SOC) enables an independent estimation of the intercalated lithium in those materials. The procedure described in Ref. [33] can be adapted to the LFP cathode, which consists in the charged state of $FePO_4$ and traces of $LiFePO_4$. Integral intensities of the 200 reflections for $FePO_4$ and $LiFePO_4$ phases were analyzed assuming lithiation-independent structure factors, unit cell volumes, molar masses and crystallographic densities summarized in Table 1. The phase fraction of $LiFePO_4$ and $FePO_4$ phases is calculated and, correspondingly, the local DoL for the cathode (scaled as DoL($LiFePO_4$)=1 and DoL($FePO_4$)=0) is obtained. During the consideration of the depth-resolved data (Sec. 2.7), the 301 couple of reflections for $FePO_4$ and $LiFePO_4$ is used instead of previously used 200 reflection due to partial overlap with the signal from polyvinylidene fluoride cell housing of the *in-situ* cell (Fig. S9). Parameters used for the calculation of the DoL in the graphite anode in fully charged state based on 001 LiC_6 and 002 LiC_{12} reflections are listed in Table 1.

4. Results and discussion

At SOC = 100 % the high-resolution neutron powder diffraction data can be described (Fig. S3) by $FePO_4$, lithiated graphites stage I and stage II, copper and aluminum current collectors as well as the steel cell housing. This observation is in good agreement with results from the literature [30,50-53]. It is worth to mention that the synchrotron data (having higher sensitivity to the LFP cathode in comparison to neutron scattering) displays a minor signal coming from $LiFePO_4$ in addition to $FePO_4$ (Fig. S4). At SOC = 0 % the neutron data reveal $LiFePO_4$ for the cathode only, while synchrotron diffraction yields a minor signal coming from $FePO_4$, too, which is attributed to the improved sensitivity of synchrotron radiation to the cathode subsystem. In neutron data, one can resolve a contribution from the lithiated graphite, seen as a low-angle tail to the 002 reflection of graphite (Fig. S3, left). This characteristic tail is attributed to a residual lithiation of the graphite anode in the discharged state. The amount of non-vanishing lithium inside the anode has been found slightly increasing upon cell fatigue [54], which is believed to be a direct consequence of the anode slippage effect [55].

To check the spatial distribution of the residual lithium inside the graphite anode in detail, a series of spatially-resolved neutron powder diffraction data are collected at different SOCs (as described in Sec. 2.1) and the in-plane lithium concentration profile is calculated.

4.1. In-situ evolution of the graphite lithiation

The evolution of the graphite lithiation in the center plane of the cylindrical LFP|C cell as a function of the SOC is presented in Fig. 1 and as an animation in the Supplementary Information section. The reconstructed data are plotted for a variety of cell capacities during charge/discharge in false colors maintaining the same color scheme. It can be seen, that at small SOCs, increased lithium concentrations exist at the very inner and very outer regions of the cylinder cell, which is attributed to systematically higher internal resistance in these regions. An inverse behavior (fully consistent with the distribution reported in [21]) has been observed at SOC = 100 %, where a well-defined plateau at DoL≈0.86 is formed in a narrow range between the very inner and very outer regions of the cylinder cell close to the current tabs. The observed behavior indicates that the electrode stripe undergoes a heterogeneous lithiation over its length: Within the plateau region, the full range of lithium intercalation into the graphite occurs with DoL ∈ [0.013 : 0.824], whereas at the cell outer region and around the center pin (at the highest distances to the current tabs) the lithium intercalation is varying within [0.073 : 0.712] and [0.046 : 0.723], respectively. A somewhat similar behavior was already found in fatigued $LiCoO_2$|C and NCA|C based high-energy cells of 18650-type [56,57], which was attributed to be a sign of heterogeneous cell aging.

As recently shown in Ref. [33], it is convenient to estimate the degree of cell heterogeneity by analyzing the histograms of the obtained lithium distributions. The histograms for selected distributions are plotted as insets in Fig. 1. The single narrow peak in the histograms corresponds to the constant lithiation plateau, where the plateau value is obtained from the peak position x_c, and the homogeneity of the plateau from the peak-width w. The peak in the histograms exhibits a clear shift of their position vs. cell charge/discharge, where in charged state the peak is located at the upper limit of the histogram, whereas for the plateau at SOC ≈ 0 the peak is located at the lower histogram limit approaching $x_c = 0$. The broadening or splitting of the peak at intermediate SOCs potentially indicates the development of heterogeneous lithiation states. In the literature [58,59] the development of heterogeneous states at intermediate SOC ranges was already reported for different cell types and needs to be examined in detail for the current case.

The analysis of the cell uniformity requires the consideration of the entire histogram and not only the plateau peak. In Ref. [33] a degree

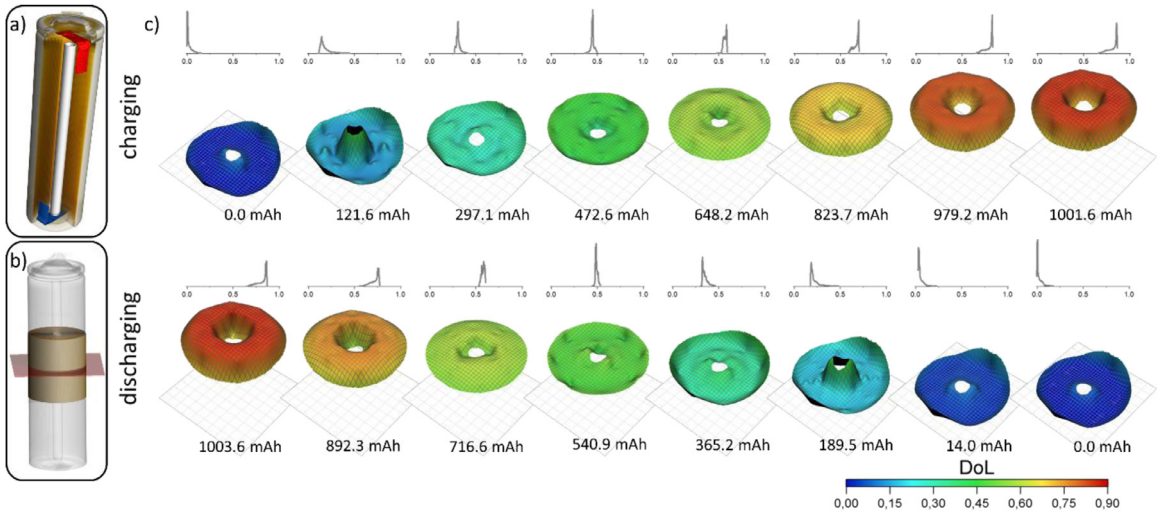

Fig. 1. Interior of the studied LFP|C cylinder-type cell as reconstructed by X-ray CT (a) and corresponding irradiated volume during high-resolution neutron diffraction (b). Evolution of in-plane 2D distribution of lithium (DoL, color coded) in the graphite anode as a function of SOC upon cell charging and discharging (c). The graphs in (c) illustrate the histograms of the distributions, x axis corresponds to DoL.

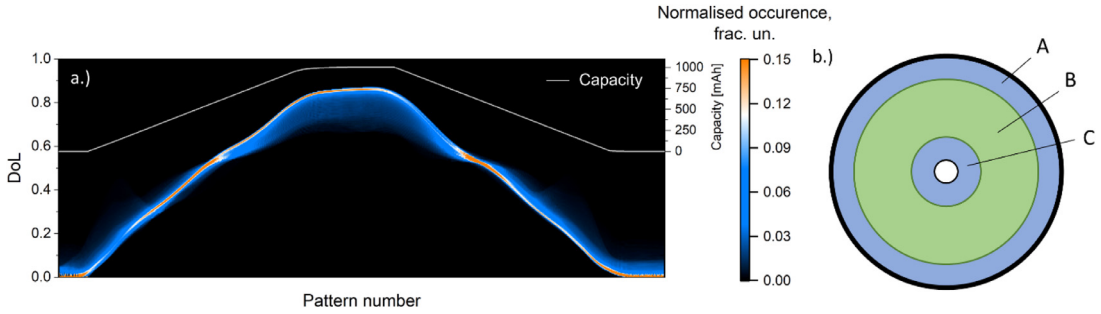

Fig. 2. Detailed evolution of the histograms of the obtained lithium-distributions (color coded) as a function of diffraction pattern/time (a) and a sketch of a lithium distribution map (b). The white line in (a) corresponds to the cell capacity as deduced from the electrochemical data.

of homogeneity corresponding to the fraction of the plateau area within the whole histogram was proposed and calculated as $\eta = A_p/A_c$, where A_p is the integral intensity of a Gauss fit to the "plateau-peak" and $A_c = \int histogram$ is the integral over the whole histogram. Fig. 2 displays the stack of the distribution histograms, where each single histogram of the individual patterns has been normalized to $\int histogram = 1$. In the discharged state (SOC ≈ 0 %) the histogram of the in-plane lithiation of the graphite anode is represented by a low-lying peak with x_c~0.002 and a tail towards higher lithium concentrations. As mentioned above, the peak corresponds to the constant-concentration plateau in the discharged state (marked as B in Fig. 2b), whereas the tail reflects the residual lithiation of the graphite at the outer cell region (A in Fig. 2b) and around the center pin (C in Fig. 2b).

Cell charging is characterized by a "collecting" of the tail from the plateau peak towards higher DoL, which can be attributed to a predominant lithiation of the low lithiated graphite in region B. At DoL=0.5 the cell displays the most homogeneous state during charging, where a kind of inflection point is observed with the lithium concentration in region B exceeding the one in regions A and C. At DoL > 0.5 the tail to the plateau peak is located at lower DoL. The observed "inflection" behavior can be associated to the potential difference required to further lithiate stage II to stage I. During cell charge, the outer cell areas are first lithiated to LiC_{12} before LiC_6 starts to form in the region close to the current lids.

The found lithiation distribution is symmetric when comparing charge and discharge. Slight differences can be attributed to cell polarization and/or asymmetric character of graphite lithiation [46,47]. It is worth to mention that the obtained details of the lithium distribution are largely smeared out by the coarse spatial resolution. Neutron diffraction is likely incapable to resolve the fine heterogeneous details on the electrode level. An improved spatial resolution can be obtained using synchrotron radiation, potentially adopting sufficiently smaller beam sizes. The use of radial oscillating collimators with synchrotron radiation is quite limited; therefore, the closest analogy to spatially-resolved neutron powder diffraction would be powder diffraction with conical slits (see Sec. 2.6). In the experiment, the diffraction signal is obtained from a series of needle-like gauge volumes (Fig. S8), from which, in turn, the in-plane lithium-distribution of the 18650-type cell is reconstructed. The obtained distribution is in good agreement to the results from the spatially-resolved neutron powder diffraction. However, the spatial resolution of X-ray diffraction using conical slits is still too coarse to resolve the electrode layers wound around the center pin. To address this question, an XRD-CT experiment is performed on the LFP|C cell in the fully charged state. Its in-plane spatial resolution of 30 μm enables to resolve single electrode stripes, thus bringing it closer to X-ray CT (Fig. S7c).

4.2. High-resolution XRD-CT probe of electrode lithiation at SOC = 100 %

The X-ray diffraction patterns collected during the XRD-CT experiment (see Sec. 2.5) enable a simultaneous localization of the different cell components. Integral diffraction intensities corresponding to the separator, Li_xFePO_4 cathode, Li_xC_6 anode and their current collectors, center pin and cell housing are reconstructed and plotted in Fig. 3a. The resolution is sufficient to resolve the double-coated electrodes, although a small overlap between the different materials at the edges of the electrodes exists, which can be attributed to a kind of partial volume effect.

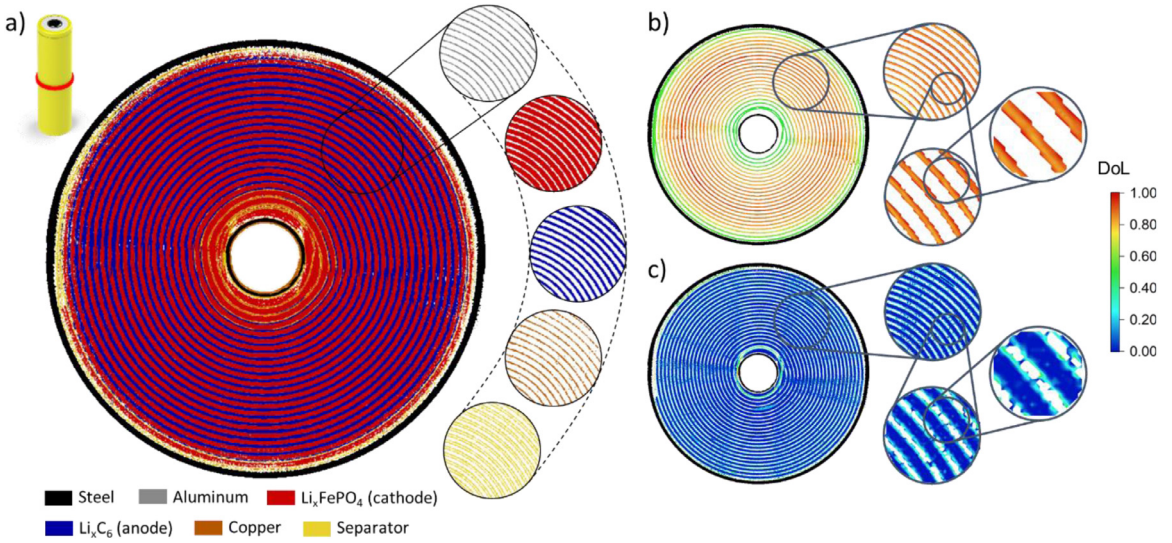

Fig. 3. Layout (a) of the studied 18650-type cell in central plane as deduced from XRD-CT experiments (different cell components: electrodes, current collectors, separator and cell housing are marked by different colors); spatially-resolved lithium content (corresponding to DoL distribution) in the anode (b) and cathode (c) of the studied 18650-type cell. For (b) and (c) a unified false color code is applied (see legend).

The obtained results are complementary to X-ray CT (Fig. S7c), where steel housing, center pin, Fe in Li_xFePO_4 and Cu current collectors are mainly contributing to the reconstructed images.

Furthermore, the lithium concentrations in the Li_xFePO_4 cathode and the Li_xC_6 anode are calculated (see Sec. 3.2). In Fig. 3b, the obtained lithium distribution in the middle plane of the charged graphite anode is shown. In general, the findings from spatially-resolved neutron powder diffraction about systematically lower lithium concentrations at the beginning and the end of the electrode stripes (regions A and C in Fig. 2b) in charged high-power LFP|C cell can also be confirmed by XRD-CT. The lithium concentration along the electrode stripe is peaking at its middle (section B in Fig. 2) close to the position of the current lid, which is consistent with the current distribution scheme proposed [21]. In selected narrow regions close to the center pin and the cell housing no signal from LiC_6 is observed, which lowers the DoL in these regions below 0.5. Analysis of the lithium distribution in the graphite across the anode stripe reveals a systematically higher lithiation of the graphite electrode towards the separator side (see inset in Fig. 3b), which was recently also reported for a single-layer cell [18].

A similar analysis of the Li_xFePO_4 cathode lithiation generally yields a more uniform lithium distribution over the entire electrode stripe. This difference can be attributed to the potential differences defining the lithiation of $LiFePO_4$ along the electrode stripe, which in contrast to the lithiated graphite has a more continuous character. Analogous to the anode, an increased lithium content at the separator side is present (see inset in Fig. 3c), corresponding to a heterogeneous lithiation across the electrode thickness. The observed heterogeneities of the lithium distribution over the electrode thickness (i.e. at the side of the separator) are in agreement with theoretical predictions [60] and experiment [18]. Their presence in a cell in a well-relaxed charged state can be attributed to the aftereffects caused by the current density distribution and, thus, creates substantial interest for further studies of the lithium distribution over the cathode electrode thickness during electrochemical intercalation and extraction of lithium.

4.3. Depth lithiation profile of Li_xFePO_4 electrode

The lithium distribution over the Li_xFePO_4 cathode thickness, extracted from a LFP|C cell similar to the previously studied one, is determined experimentally, applying the methodology described in Sec. 2.7. A sketch of the electrochemical LFP|Li cell used in the experiment is shown in Fig. 4a. The lithium concentration x in Li_xFePO_4 is estimated in a similar way as in the XRD-CT experiment and its evolution over thickness and time is shown in Fig. 4b. At first glance, the lithiation front in Li_xFePO_4 (represented as the degree of lithiation $DoL(d,t)$) perfectly reflects the cell capacity. Splitting the $DoL(d,t)$ into the thickness-averaged but time-dependent part $\overline{DoL(t)}$ and a fluctuation part $\Delta DoL(d,t)$

$$DoL(d,t) = \overline{DoL(t)} + \Delta DoL(d,t) \tag{2}$$

reveals two distinctly different states of lithiation gradient separating for the charged and discharged states (Fig. 4c). At a SOC below ≈20 % (corresponding to a lithiated cathode) the lithium distribution across the electrode can be considered as uniform. Further cell charging (from 20 % to 50 %) results in the development of weak non-uniformities in the Li-distribution, i.e. 60 µm of the LFP electrode at the current collector side show increased lithium concentrations, whereas the first 20 µm at the separator side display a slightly lower lithiation. The situation inverts at ca. 50 % capacity level, where the lithium distribution in the LFP cathode separates into a lithium-depleted region (at the side of current collector) and a lithium-rich region (at the side of separator) with nearly identical thicknesses existing over a broad capacity range. Inverting the current direction (charging to discharging) also reverses the distribution to the initial state.

The observed heterogeneous cathode lithiation in the charged state agrees with the lithiation gradient observed by the XRD-CT experiment. The presence of the lithium-rich region in the cathode at the separator side in the charged state can be attributed to the local current density distribution [18], representing the surface ion flux and reflecting the rates of electrochemical reactions. Generally, the results are in fair agreement with the theoretical model reported in Ref. [60].

5. Summary

The lithiation kinetics of the positive and negative electrode materials in a commercial LFP|C 18650-type lithium-ion battery are investigated using various diffraction-based techniques, X-ray computed tomography and electrochemical characterization. The lithium distribution in the cathode and anode are probed at different SOCs and at different length scales, where it is found, that heterogeneities of the lithium distribution appear over length, height and thickness of the electrode stripes.

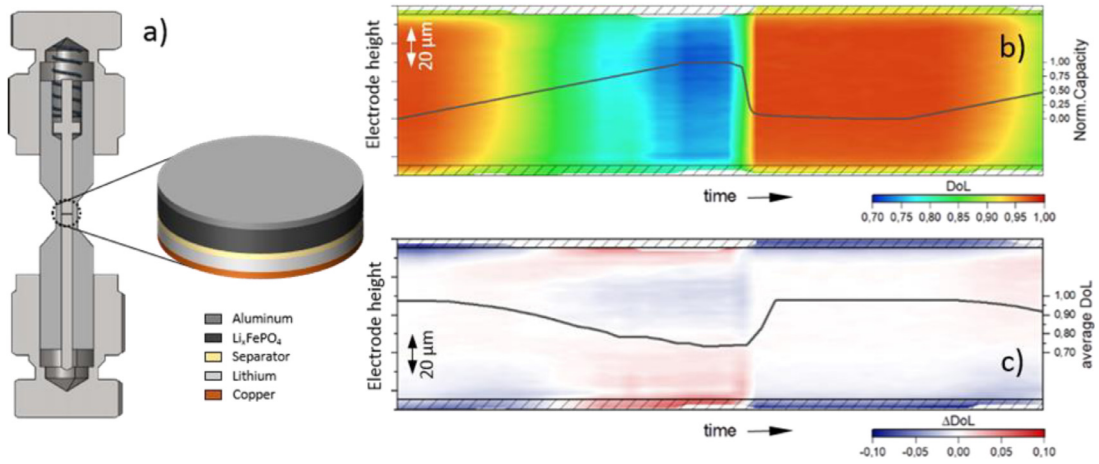

Fig. 4. Schematic of the in-situ cell (a) and lithium concentration (in terms of local DoL presented by false colors) through the thickness of the LFP cathode vs. cycling (b) as obtained from depth-resolved XRD scans using µm-sized beam (Section 2.7). Corresponding DoL fluctuations after subtraction of $\overline{DoL(t)}$ (c). Black lines represent instantaneous cell capacity. Shaded regions illustrate edge effects associated with the electrode surfaces and corresponding roughness.

The non-uniformities of the lithium distribution persist in the whole range of the cell operation, where the lithiation profiles at SOC = 0 % and SOC = 100 % display an inverted behavior. Considering the lithiation along the anode stripe, systematically lower lithium concentrations at both ends of the anode can be observed compared to the middle part of the stripe closer to the current tabs. All this leads to a heterogeneous "lithiation stress" distribution within the cell, where at the outer/inner cell region the degree of lithiation is modified from 0.049/0.046 at SOC = 0% to 0.713/0.725 at SOC 100%, whilst in the plateau region at the middle part of the anode stripe shows a change in the lithiation from 0.002 to 0.844. These non-uniform distributions will certainly affect cycling stability, aging characteristics, heterogeneity, safety and lifetime. A higher lithiation grade in the middle of the anode is confirmed using a non-destructive spatial characterization with 30 µm–scale resolution. The lithiation of the cathode is generally more uniform along the electrode stripe, whilst lithium gradients are also observed through the electrode thickness at SOC = 100 %. Systematically higher lithiation of the anode and the cathode at the side of the separator is observed. The presence of a lithium gradient through the electrode thickness is a direct consequence of its current density distribution, which optimization is extremely crucial for the cell performance and especially for the optimization of the charging profile in high-power cells.

The increased lithium concentration towards the separator is confirmed in a model system built on a single cathode layer, where lithium-depleted and lithium-rich regions are clearly resolved in the charged state. These observations are in line with the experimental findings reported in the literature and also with the results of theoretical simulations. Methods capable of monitoring the lithium distribution throughout the electrode thickness open up very interesting perspectives for its control and manipulation, such as using an engineered current density profile through adopted electrode morphology.

Declaration of Competing Interest

The authors declare that they have no known competing financial interests or personal relationships that could have appeared to influence the work reported in this paper.

CRediT authorship contribution statement

Dominik Petz: Data curation, Formal analysis, Visualization, Writing – original draft. **Martin J. Mühlbauer:** Methodology, Investigation, Validation. **Volodymyr Baran:** Investigation. **Alexander Schökel:** Investigation, Methodology. **Vladislav Kochetov:** Visualization, Data curation, Formal analysis, Software. **Michael Hofmann:** Resources, Methodology. **Vadim Dyadkin:** Formal analysis, Software. **Peter Staron:** Resources, Methodology. **Gavin Vaughan:** Resources, Methodology. **Ulrich Lienert:** Resources, Methodology. **Peter Müller-Buschbaum:** Funding acquisition, Writing – review & editing. **Anatoliy Senyshyn:** Writing – review & editing, Project administration, Methodology.

Acknowledgment

The authors acknowledge the access to the research infrastructure of the Heinz Maier-Leibnitz Zentrum (MLZ) and the ESRF-The European Synchrotron. We acknowledge DESY (Hamburg, Germany), a member of the Helmholtz Association HGF, for the provision of experimental facilities. Parts of this research were carried out at PETRA III beamlines P02.1, P21.2 and P07, the latter operated by Hereon. The study was supported in part by German Ministry of Education and Science (Projects 05K16VK2 and 05K19VK3), Heinz Maier-Leibnitz Zentrum and Karlsruhe Institute of Technology. Authors wish to thank Dr. W. Gan (Helmholtz-Zentrum Hereon), Dr. J. Rebello-Kornmeier (MLZ), J. Krüger (MLZ) for their assistance with spatially-resolved neutron diffraction experiments at STRESS-SPEC; Dr. M. di Michel (ESRF), E. Tarajan (MathWorks) for the fruitful discussion and advices; J. Pfanzelt (MLZ) for the help with construction and built-up of custom electrochemical cell.

Supplementary materials

Supplementary material associated with this article can be found, in the online version, at doi:10.1016/j.ensm.2021.06.028.

References

[1] J.M. Tarascon, M. Armand, Issues and challenges facing rechargeable lithium batteries, Nature 414 (6861) (2001) 359–367.
[2] M. Armand, J.M. Tarascon, Building better batteries, Nature 451 (7179) (2008) 652–657.
[3] C.R. Birkl, et al., Degradation diagnostics for lithium ion cells, J. Power Sources 341 (2017) 373–386.
[4] M.J. Mühlbauer, et al., Probing chemical heterogeneity of Li-ion batteries by in operando high energy X-ray diffraction radiography, J. Power Sources 403 (2018) 49–55.
[5] S. Müller, et al., Quantifying inhomogeneity of lithium ion battery electrodes and its influence on electrochemical performance, J. Electrochem. Soc. 165 (2) (2018) A339–A344.
[6] J. Lei, F. McLarnon, R. Kostecki, In situ Raman microscopy of individual LiNi0.8Co0.15Al0.05O2 particles in a Li-ion battery composite cathode, J. Phys. Chem. B 109 (2) (2005) 952–957.

[7] J.E. Owejan, et al., Solid electrolyte interphase in Li-ion batteries: evolving structures measured in situ by neutron reflectometry, Chem. Mater. 24 (11) (2012) 2133–2140.
[8] C.A. Bridges, et al., In situ observation of solid electrolyte interphase formation in ordered mesoporous hard carbon by small-angle neutron scattering, J. Phys. Chem. C 116 (14) (2012) 7701–7711.
[9] D.P. Finegan, et al., Investigating lithium-ion battery materials during overcharge-induced thermal runaway: an operando and multi-scale X-ray CT study, PCCP 18 (45) (2016) 30912–30919.
[10] R.F. Ziesche, et al., 4D imaging of lithium-batteries using correlative neutron and X-ray tomography with a virtual unrolling technique, Nat. Commun. 11 (1) (2020) 777.
[11] A. Senyshyn, et al., In-operando" neutron scattering studies on Li-ion batteries, J. Power Sources 203 (2012) 126–129.
[12] O.J. Borkiewicz, et al., Best practices for operando battery experiments: influences of X-ray experiment design on observed electrochemical reactivity, J. Phys. Chem. Lett. 6 (11) (2015) 2081–2085.
[13] L. Cai, et al., In-situ observation of inhomogeneous degradation in large format Li-ion cells by neutron diffraction, J. Power Sources 236 (2013) 163–168.
[14] W.A. Paxton, Z. Zhong, T. Tsakalakos, Tracking inhomogeneity in high-capacity lithium iron phosphate batteries, J. Power Sources 275 (2015) 429–434.
[15] K. Kino, et al., First Imaging Experiment of a Lithium Ion Battery by a Pulsed Neutron Beam at J-PARC/MLF/BL09, in: Proceedings of the 10th World Conference on Neutron Radiography (Wcnr-10), 69, 2015, pp. 612–618.
[16] A. Senyshyn, et al., Spatially resolved in operando neutron scattering studies on Li-ion batteries, J. Power Sources 245 (2014) 678–683.
[17] G. Harding, J. Kosanetzky, U. Neitzel, X-ray diffraction computed tomography, Med. Phys. 14 (4) (1987) 515–525.
[18] D.P. Finegan, et al., Spatial dynamics of lithiation and lithium plating during high-rate operation of graphite electrodes, Energy Environ. Sci. 13 (8) (2020) 2570–2584.
[19] D.P. Finegan, et al., Spatially resolving lithiation in silicon–graphite composite electrodes via in situ high-energy X-ray diffraction computed tomography, Nano Lett. 19 (6) (2019) 3811–3820.
[20] D.P. Finegan, et al., Spatial quantification of dynamic inter and intra particle crystallographic heterogeneities within lithium ion electrodes, Nat. Commun. 11 (1) (2020) 631.
[21] A. Senyshyn, et al., Homogeneity of lithium distribution in cylinder-type Li-ion batteries, Sci. Rep. 5 (2015) 18380.
[22] M. Mühlbauer, et al., Inhomogeneous distribution of lithium and electrolyte in aged Li-ion cylindrical cells, J. Power Sources 475 (2020) 228690.
[23] Y.D. Liu, et al., Failure study of commercial LiFePO4 cells in over-discharge conditions using electrochemical impedance spectroscopy, J. Electrochem. Soc. 161 (4) (2014) A620–A632.
[24] S. Panchal, et al., Electrochemical thermal modeling and experimental measurements of 18650 cylindrical lithium-ion battery during discharge cycle for an EV, Appl. Therm. Eng. 135 (2018) 123–132.
[25] S.J. Drake, et al., Measurement of anisotropic thermophysical properties of cylindrical Li-ion cells, J. Power Sources 252 (2014) 298–304.
[26] Q. Liu, et al., Rate-dependent, Li-ion insertion/deinsertion behavior of LiFePO4 cathodes in commercial 18650 LiFePO4 cells, ACS Appl. Mater. Interfaces 6 (5) (2014) 3282–3289.
[27] H. He, et al., Dynamic lithium intercalation/deintercalation in 18650 lithium ion battery by time-resolved high energy synchrotron X-ray diffraction, J. Electrochem. Soc. 162 (10) (2015) A2195–A2200.
[28] Q. Liu, et al., Capacity fading mechanism of the commercial 18650 LiFePO4-based lithium-ion batteries: an in situ time-resolved high-energy synchrotron XRD study, ACS Appl. Mater. Interfaces 10 (5) (2018) 4622–4629.
[29] William A. Paxton, Z.Z., Thomas Tsakalakos, In-situ energy-dispersive X-ray diffraction study of a commercial lithium iron phosphate/graphite 18650 cell, Adv. X-Ray Anal. 58 (2015) 137–145.
[30] N. Paul, et al., Aging behavior of lithium iron phosphate based 18650-type cells studied by in situ neutron diffraction, J. Power Sources 345 (2017) 85–96.
[31] F.B. Spingler, M. Naumann, A. Jossen, Capacity recovery effect in commercial LiFePO4/graphite cells, J. Electrochem. Soc. 167 (4) (2020).
[32] Heinz Maier-Leibnitz Zentrum, STRESS-SPEC: Materials science diffractometer, Journal of large-scale research facilities 1 (2015).
[33] D. Petz, et al., Heterogeneity of graphite lithiation in state-of-the-art cylinder-type Li-ion cells, Batter. Supercaps 4 (2) (2021) 251.
[34] Hoelzel, M., et al., High-resolution neutron powder diffractometer SPODI at research reactor FRM II. Nuclear instruments & methods in physics research section a-accelerators spectrometers detectors and associated equipment, 2012. 667: p. 32-37. 10.1016/j.nima.2011.11.070, https://www.sciencedirect.com/science/article/pii/S0168900211021383.
[35] M. Hoelzel, A. Senyshyn, O. Dolotko, SPODI: High resolution powder diffractometer, J. Large-Scale Res. Facil. JLSRF 1 (2015) A5.
[36] C.A. Schneider, W.S. Rasband, K.W. Eliceiri, NIH Image to ImageJ: 25 years of image analysis, Nat. Methods 9 (7) (2012) 671–675.
[37] J. Wright, C. Giacobbe, M. Majkut, New opportunities at the Materials Science Beamline at ESRF to exploit high energy nano-focus X-ray beams, Curr. Opin. Solid State Mater. Sci. 24 (2) (2020) 100818.
[38] A.C. Dippel, et al., Beamline P02.1 at PETRA III for high-resolution and high-energy powder diffraction, J. Synchrotron Radiat. 22 (2015) 675–687.
[39] V. Dyadkin, et al., A new multipurpose diffractometer PILATUS@SNBL, J. Synchrotron Radiat. 23 (3) (2016) 825–829.
[40] C. Prescher, V.B. Prakapenka, DIOPTAS: a program for reduction of two-dimensional X-ray diffraction data and data exploration, High Pressure Res. 35 (3) (2015) 223–230.
[41] G.B.M. Vaughan, et al., ID15A at the ESRF - a beamline for high speed operando X-ray diffraction, diffraction tomography and total scattering, J. Synchrotron Radiat. 27 (2) (2020) 515–528.
[42] A. Vamvakeros, et al., Interlaced X-ray diffraction computed tomography, J. Appl. Crystallogr. 49 (2) (2016) 485–496.
[43] Schell, N., et al., *The high energy materials science beamline (HEMS) at PETRA III*. Vol. 772. 2013. 57-61. https://doi.org/10.4028/www.scientific.net/MSF.772.57, https://www.scientific.net/MSF.772.57.
[44] P. Staron, et al., Depth-resolved residual stress analysis with high-energy synchrotron X-rays using a conical slit cell, Mater. Sci. Forum 768-769 (2014) 72–75.
[45] Z. Hegedüs, et al., Imaging modalities at the Swedish Materials Science beamline at PETRA III, IOP Conference Series: Materials Science and Engineering, 580, 2019.
[46] A. Senyshyn, et al., Lithium intercalation into graphitic carbons revisited: experimental evidence for twisted bilayer behavior, J. Electrochem. Soc. 160 (5) (2013) A3198–A3205.
[47] C. Didier, et al., Phase evolution and intermittent disorder in electrochemically lithiated graphite determined using in operando neutron diffraction, Chem. Mater. 32 (6) (2020) 2518–2531.
[48] R. Jenkins, R. Snyder, Quantitative Analysis, in: Introduction to X-ray Powder Diffractometry, 1996, pp. 355–387.
[49] S.D.M. Jacques, et al., Pair distribution function computed tomography, Nat. Commun. 4 (2013) 2536.
[50] G. Liang, et al., Understanding rechargeable battery function using in operando neutron powder diffraction, Adv. Mater. 32 (18) (2020) 1904528.
[51] N. Sharma, et al., Direct evidence of concurrent solid-solution and two-phase reactions and the nonequilibrium structural evolution of LiFePO4, J. Am. Chem. Soc. 134 (18) (2012) 7867–7873.
[52] C.-W. Hu, et al., Real-time investigation of the structural evolution of electrodes in a commercial lithium-ion battery containing a V-added LiFePO4 cathode using in-situ neutron powder diffraction, J. Power Sources 244 (2013) 158–163.
[53] D. Goonetilleke, et al., Structural evidence for Mg-doped LiFePO4 electrode polarisation in commercial Li-ion batteries, J. Power Sources 394 (2018) 1–8.
[54] O. Dolotko, et al., Fatigue process in Li-ion cells: an in situ combined neutron diffraction and electrochemical study, J. Electrochem. Soc. 159 (12) (2012) A2082–A2088.
[55] A.J. Smith, et al., Interpreting high precision coulometry results on Li-ion cells, J. Electrochem. Soc. 158 (10) (2011) A1136–A1142.
[56] M.J. Muhlbauer, et al., Effect of fatigue/ageing on the lithium distribution in cylinder-type Li-ion batteries, J. Power Sources 348 (2017) 145–149.
[57] D. Petz, et al., Lithium heterogeneities in cylinder-type Li-ion batteries – fatigue induced by cycling, J. Power Sources 448 (2020) 227466.
[58] S.V. Erhard, et al., Simulation and measurement of the current density distribution in lithium-ion batteries by a multi-tab cell approach, J. Electrochem. Soc. 164 (1) (2017) A6324–A6333.
[59] P.J. Osswald, et al., Current density distribution in cylindrical Li-Ion cells during impedance measurements, J. Power Sources 314 (2016) 93–101.
[60] M. Wang, et al., The effect of local current density on electrode design for lithium-ion batteries, J. Power Sources 207 (2012) 127–133.